RESEARCH ARTICLE

A study of the three-dimensional spectral energy distribution in a zero pressure gradient turbulent boundary layer

J. LeHew · M. Guala · B. J. McKeon

Abstract Time-resolved particle image velocimetry (PIV) measurements performed in wall parallel planes at three wall normal locations, $y^+ = 34$, 108, and 278, in a zero pressure gradient turbulent boundary layer at $Re_\tau = 470$ are used to illuminate the distribution of streamwise velocity fluctuations in a three-dimensional energy spectrum (2D in space and 1D in time) over streamwise, spanwise, and temporal wavelengths. Two high-speed cameras placed side by side in the streamwise direction give a $10\delta \times 5\delta$ streamwise by spanwise field of view with a vector spacing of $\Delta x^+ = \Delta z^+ \approx 37$ and a time step of $\Delta t^+ = 0.5$. Although 3D wavenumber–frequency spectra have been calculated in acoustics studies, to the authors' knowledge this is the first time they has been calculated and presented for a turbulent boundary layer. The calculation and normalization of this spectrum, its relation to 2D and 1D spectra, and the effects of the PIV algorithm on its shape are carefully analyzed and outlined.

M. Guala worked on this project at the California Institute of Technology but is currently at the University of Minnesota.

J. LeHew · M. Guala (✉) · B. J. McKeon
Graduate Aerospace Laboratories,
California Institute of Technology,
1200 E. California Blvd. MC 205-45,
Pasadena, CA 91125, USA
e-mail: mguala@umn.edu

J. LeHew
e-mail: lehew@caltech.edu

Present Address:
M. Guala
Department of Civil Engineering,
University of Minnesota, 500 Pillsbury Drive S.E,
Minneapolis, MN 55455, USA

1 Introduction

The current understanding of the structural and statistical nature of the turbulent boundary layer over a large range of Reynolds number rests primarily upon spatial information from direct numerical simulations (DNS) and particle image velocimetry (PIV) experiments, and temporal information from experimental measurements at a single point, yet there is a lack of simultaneous temporal and spatial measurements to describe the time evolution of the structures and statistics of the flow. While temporal information can be extracted from DNS data, not only is the range of Reynolds numbers limited, but the computational resources required to analyze a time-resolved flow over a sufficiently long time period would be enormous. Similarly, in experiments, most commonly used instruments, such as hot wire anemometers, only provide temporal information at a single point, where the recovery of spatial information requires the arduous task of taking measurements at two or more points simultaneously over a range of separations. Planar PIV measurements provide a 2D spatial representation of the flow and with a sufficiently high frame rate, as shall be discussed, provide simultaneous spatial and temporal measurements allowing a statistical and structural analysis of the turbulent boundary layer over two spatial dimensions and time.

Often, when either the spatial or temporal information is not acquired, a conversion between the two is performed using Taylor's frozen turbulence hypothesis (Taylor 1938), which states that the spatial field can be reconstructed from the temporal field if the convection velocities of the individual eddies or scales which compose the flow are known. This conversion is performed assuming the eddies are "frozen", or in other words, that their shape does not evolve significantly over the distance projected. While the

convection velocity of all such eddies is usually assumed to be equal to the local mean velocity, many studies have shown that this is not always a valid assumption (Morrison et al. 1971; Kim and Hussain 1993; Krogstad et al. 1998; Chung and McKeon 2010; del Álamo and Jiménez 2009; LeHew et al. 2010). A recent example of the importance of knowing the correct conversion was demonstrated by Monty and Chong (2009) who compare channel flow computations and experiments under the same conditions using the spatial spectrum from computations and the converted temporal spectrum from experiments. The discrepancies between the spatial and temporal spectra were put into better agreement using a scale-dependent convection velocity near the wall. In the PIV measurements presented in this paper, information is recorded in both time and space, so no conversion is necessary, and it is possible to test the validity of Taylor's hypothesis at all measurement locations.

The use of time-resolved PIV to address the need for both spatial and temporal measurements in the turbulent boundary layer was first considered by Dennis and Nickels (2008) at a wall normal location of $y/\delta = 0.16$, where δ is the boundary layer thickness. It was concluded that at this particular wall normal location with a 6δ streamwise field of view, Taylor's hypothesis holds, although deviation was noted between the actual and projected velocity fields at distances beyond 4δ downstream. Based on the works cited previously, a more notable deviation would likely appear with measurements both very near and far from the wall, which will be addressed in the current study over a larger spatial field and considering the entire (k_x, k_z, ω) domain.

Although the use of PIV for simultaneous spatial and temporal measurements of a turbulent boundary layer is promising, there are a number of issues to be addressed. First, the resolution of the spatial fluctuations of the flow, and thus the resolution of the spatial spectrum, is limited by the interrogation window size, which attenuates small-scale fluctuations on the order of the window size as noted by Willert and Gharib (1991). A technique to determine the optimal window size, considering both the attenuation from the interrogation window and the noise introduced by the PIV algorithm, was proposed by Foucaut et al. (2004). An outline of all of the effects of PIV on the spatial spectrum including methods for avoiding spectral leakage and aliasing in space is presented by Tomkins and Adrian (2005). The study of the space–time correlation in hot and cold jet flows by Wernet (2007) discusses the need for oversampling and low-pass filtering in time to avoid temporal aliasing of PIV data. Finally, not only should the smallest energetic scales in the flow be recovered, but also the largest scales found to extend up to 14 times the pipe radius in experiments by Kim and Adrian (1999). For boundary layer measurements, both the large-scale motions (LSMs)

with an energetic peak at $\lambda_x = 2 - 3\delta$ and the superstructures, with an energetic peak at $\lambda_x = 6\delta$ as discussed by Hutchins and Marusic (2007), Monty et al. (2009), and Guala et al. (2011), where λ_x is the streamwise wavelength, must be resolved. As discussed by Balakumar and Adrian (2007), streamwise scales longer than 3δ at all wall normal locations and Reynolds numbers considered contain at least 45% of the turbulent kinetic energy in the zero pressure gradient boundary layer. In addition, Ganapathisubramani et al. (2003) found that hairpin packets of comparable streamwise extent contain a significant amount of Reynolds stress, $-\overline{uv}$, and thus these large scales must be resolved to accurately represent the flow. As noted by Monty et al. (2009), while the 6δ superstructure peak becomes almost undiscernable outside the log layer, near the wall this peak is prominent and structures of this size and even larger must be resolved to fully encompass the near wall energy and dynamics.

The goal of the current work is to study the flow physics in wall parallel planes throughout the boundary layer using the 1D, 2D, and, for the first time, 3D (2D in space, 1D in time) streamwise velocity spectra over all combinations of frequency, and streamwise and spanwise wavenumbers. For this purpose, time-resolved PIV measurements were performed at $y^+ = 34, 108, 278 (y/\delta = 0.07, 0.23, 0.59)$ to illuminate the differences between the near wall, outer log layer, and wake regions of the boundary layer. The quantity $y^+ = y\, u_\tau/\nu$ is the inner-scaled, non-dimensional, wall normal distance where $u_\tau = \sqrt{\tau_w/\rho}$ is the friction velocity, τ_w is the shear stress at the wall, ρ is the fluid density, and ν is the kinematic viscosity. In Sect. 2, the experimental setup and choice of PIV processing parameters are described. The mean statistics are then presented in Sect. 3 and compared to the literature. The effect of the PIV processing on both the velocity signal and spectral calculations is carefully outlined following the work of Tomkins and Adrian (2005), and steps for calculating the 3D spectrum and its relation to an ideally measured spectrum are presented in Sect. 4. This is followed by a presentation and discussion of the spectra in Sect. 5. Finally, the results are summed up in Sect. 6.

2 Experimental setup

Measurements of a zero pressure gradient boundary layer developing over a flat plate were performed on a 1.1 m long by 0.45-m-wide Plexiglass plate with an elliptical leading edge and an adjustable wedge-shaped trailing edge flap situated in a 2m long by 1-m-wide test section of a free surface water tunnel facility. The 13.9-mm-thick boundary layer on the bottom of the plate was studied to avoid interaction with surface waves. A shroud with a wedge-
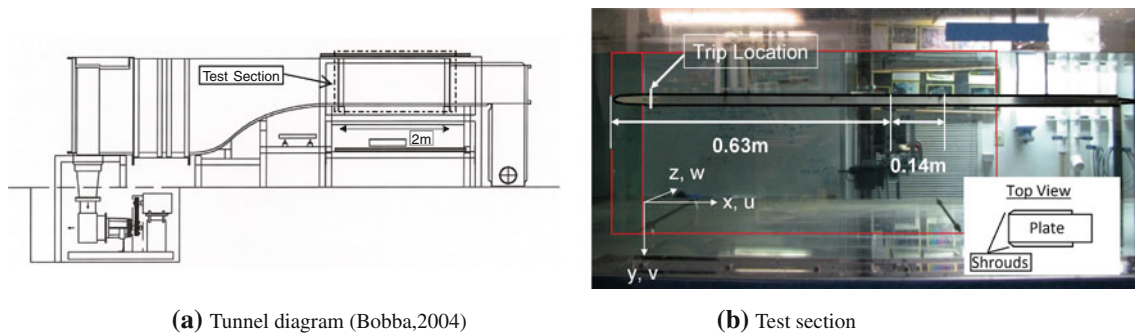
(a) Tunnel diagram (Bobba,2004)

(b) Test section

Fig. 1 a Water tunnel schematic showing the location of the test section. **b** Photograph of the test section where the red lines outline the submerged portion of the shroud and its wedge-shaped leading edge. A *top down* view is provided in the *inset* to clarify the shroud orientation

shaped leading edge was placed along the sides of the plate to promote a two-dimensional flow. A thin strip of tape (approximately 3 mm long, 0.25 mm thick, and spanning the width of the plate) was placed immediately downstream of the elliptical leading edge on the measurement side to promote transition and favor the establishment of a turbulent regime at the measurement location. The flow was conditioned by passing it through a perforated plate, a honey comb, three turbulence reducing screens, and finally a 6:1 contraction. Measurements were made starting 0.63 m downstream of the leading edge. The free stream velocity was 0.67 m/s, and the free stream turbulence level was less than 0.1%. The free stream velocity, and thus Reynolds number, for these experiments was set to provide the best flow conditions possible and to allow a small enough displacement per frame for accurate PIV mesurements. It should be noted that this choice led to a relatively low Reynolds number, $Re_\tau = 470$, which limits the scale separation observable in these experiments. A diagram of the tunnel and a photograph showing the test section and coordinate system are presented in Fig. 1.

Time-resolved 2D PIV was used to measure the flow field in the wall normal and wall parallel directions in two separate experiments using a LaVision PIV system with 2 Photron Fastcam APX-RS high-speed cameras equipped with Tamron SP AF 180 mm F/5.5 macro lenses. The cameras acquired images at 2,000 frames per second with $1,024 \times 1,024$ pixel resolution for all experiments. The flow was seeded with 10-μm hollow glass spheres with a specific gravity of 1.1. The seeding density was similar in both wall normal and wall parallel measurements, and the average particle image diameter was 2.2 and 3.1 pixels, respectively. The flow was illuminated by a Photonics DM20-527 solid-state laser providing 20 mJ/pulse with a sheet thickness of approximately 1 mm. The sheet was thick enough to nearly eliminate out-of-plane loss with $|\hat{v}|\Delta t/y_0 < 0.04$, much less than the maximum allowable value of 0.25 suggested by Keane and Adrian (1990), where y_0 is the laser sheet thickness, Δt is the time between
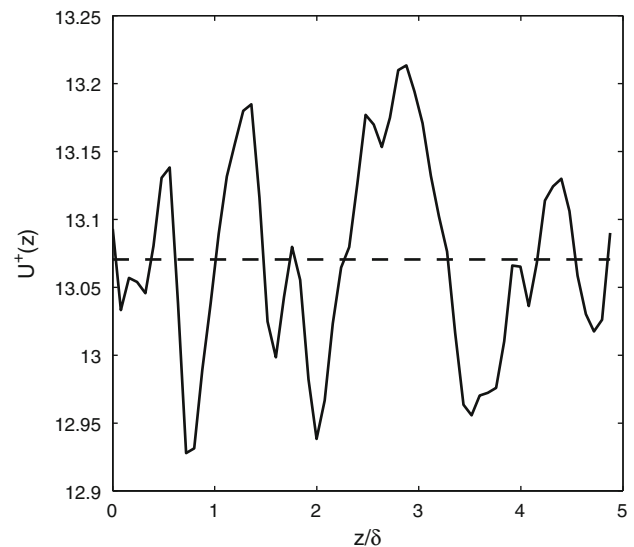

Fig. 2 The spanwise variation of the velocity averaged over the streamwise direction and time at $y^+ = 34$

images, and $\hat{v}$ is the out-of-plane velocity estimated from the rms velocity fluctuations. The two-dimensionality of the flow in wall parallel planes is verified in Fig. 2 showing the velocity averaged over the streamwise direction and time for $y^+ = 34$. For this plane, the local mean streamwise velocity at a given spanwise location varied from the global mean by no more than 1%. The spanwise variation of velocity is similar at the other two wall normal locations.

2.1 Measurements

Wall normal measurements were taken first to characterize the flow at the start of the measurement location using only one camera. The field of view was 50.6 mm × 50.6 mm ($L_x \times L_y$). Due to camera memory limitations, a maximum of 2,048 images could be taken at a time. For collapse of the mean profile, 5 experiments were performed.

For wall parallel measurements, two cameras were placed side by side in the streamwise direction with a

10–20 pixel overlap producing a total field of view of approximately 140 mm × 70 mm ($L_x \times L_z$) with some slight deviation between the three planes investigated. A laser sheet was guided into the test section parallel to the flat plate and was centered at locations 1, 3.2, and 8.2 mm from the wall in order to capture the near wall, outer log layer, and wake regions of the turbulent boundary layer. For each plane, 40 experiments were performed providing over 80,000 instantaneous realizations allowing collapse of the calculated power spectra.

2.2 Vector processing

The velocity field calculations for both the wall normal and wall parallel planes were performed using LaVision's Davis software. In the case of the wall parallel planes, the vector fields were stitched together after processing. To assure an exact overlap of the processed fields, the original images were cropped before processing to ensure overlap of an integer number of interrogation windows after processing. In addition, due to bubbles and particles occasionally aggregating at the wall, for the plane nearest the wall, an average over all images was taken and subtracted from each raw image before vector calculation to reduce the effects of stationary tracers on this calculation.

A 50% overlap of interrogation windows was used to satisfy the Nyquist criterion, which, as will be discussed in Sect. 4, is necessary to resolve the spectrum properly. The correlation peak fitting was done using a Gaussian three-point estimator in each coordinate direction independently; Whittaker reconstruction was used for image reconstruction, and in-plane particle pair loss was minimized using a window shift. For wall normal measurements, the window size was reduced from 16 × 16 to 12 × 12 pixels over two passes. For wall parallel measurements both passes were performed with a 32 × 32 pixel window with each camera processed separately. The non-dimensional vector spacing, field size, and wall normal locations are summarized in Table 1.

After the initial vector calculation, spurious vectors were removed and replaced via interpolation. In all images, less than 3% of the vectors were removed so the effect of interpolation on the measurements was considered minimal.

While the wall normal data were smoothed with a 3 × 3 filter, no smoothing was performed in wall parallel planes as to preserve the fluctuating velocity signal and spectral shape.

3 Flow properties and statistics

The mean velocity profile and boundary layer thickness were calculated from the wall normal measurements averaged in the nearly homogeneous streamwise direction over all frames and over all experiments. The boundary layer thickness, calculated using the $U(y) = 0.99U_\infty$ criterion, varied by 5% over the 50-mm window. The mean profile is compared with the experiments of DeGraaff and Eaton (2000) at a similar Reynolds number ($Re_\theta = \theta U_\infty / v = 1{,}430$) in Fig. 3a. θ is the momentum thickness, and U_∞ is the free stream velocity.

Since no direct measurements of the wall shear stress were made in this experiment, the friction velocity was calculated from a least squares fit to the predetermined log layer marked with circles in Fig. 3a. All of the flow parameters are summarized in Table 1.

In the wall parallel measurements, δ changed by about 10% over the whole field of view. While the outer scale, y/δ, is not constant over the measurement plane, the inner-scaled wall distance is nearly constant since u_τ only decreases weakly with streamwise extent. Thus, each plane of the wall parallel data is representative of a particular inner-scaled distance from the wall. Data will also be presented using an averaged outer scale in some cases for convenience.

The rms streamwise velocity fluctuations for each wall parallel plane are presented in Fig. 3b and match closely with the data from DeGraaff and Eaton (2000) and Erm and Joubert (1991). Any small deviation from the literature values may be from the spatial averaging present in the PIV calculations as discussed in Sect. 4. The wall normal fluctuations measured in the wall normal plane are also presented for completeness and deviate from the data shown, particularly near the wall. This deviation arises from limited resolution in the wall normal plane and is also observed in the streamwise velocity fluctuations in this plane. As already noted, this is not an issue in the wall parallel planes, which will be the focus of all discussions from here on.

Table 1 Experimental parameters

Re_τ	Re_θ	δ	θ	U_∞	u_τ	v/u_τ	Δy^+	Δt^+
470	1,280	13.9 mm	1.72 mm	0.67 m/s	0.03 m/s	29.5 μm	10.0	0.5
Plane	y^+	y/δ	U^+	U/U_∞	u_{rms}^+	$\Delta x^+, \Delta z^+$	L_x/δ	L_z/δ
1	34	0.07	13.1	0.59	2.10	37.6	9.98	4.91
2	108	0.23	16.4	0.73	1.53	37.1	9.85	4.84
3	278	0.59	20.2	0.90	1.25	37.5	10.03	4.89

(a) Mean profile
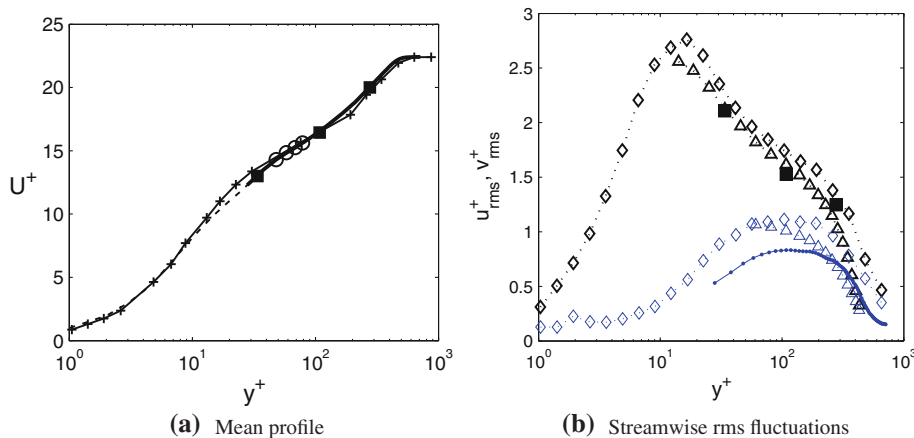

(b) Streamwise rms fluctuations

Fig. 3 In **a** the mean velocity profile is presented where the symbols are: *solid line* mean profile from wall normal measurements; *square* mean velocity from wall parallel measurements; *dashed line* Spalding fit (Spalding 1961); (+) data from DeGraaff and Eaton (2000) at $Re_\theta = 1,430$; *circle* points selected to represent the log layer. In **b** *black lines and symbols* are for u_{rms}^+ and *blue lines and symbols* are for

v_{rms}^+. The symbols are: *square* u_{rms}^+ from wall parallel plane measurements; *line with circles* v_{rms}^+ from the wall normal plane measurements; *diamond* data from DeGraaff and Eaton (2000) at $Re_\theta = 1,430$; *triangle* data from Erm and Joubert (1991) at $Re_\theta = 1,003$

4 Calculation of the power spectral density in wall parallel planes

The power spectral density is defined as the Fourier transform of the correlation function of the velocity fluctuations, where the relevant non-normalized 3D correlation function is defined in Eq. 1.

$$R_{u_i u_j}(\rho_x, \rho_z, \tau) = \langle u(x, z, t) u(x + \rho_x, z + \rho_z, t + \tau) \rangle \quad (1)$$

In the above equation, ρ_x and ρ_z are the separation between points in the streamwise and spanwise directions, respectively, τ is a separation in time, the subscripts i and j represent velocity components, and the triangle brackets represent an ensemble average. The Fourier transform pair relating the correlation function to the power spectrum Θ is given in Eqs. 2 and 3.

$$\Theta_{u_i u_j}(k_x, k_z, \omega)$$
$$= \frac{1}{(2\pi)^3} \iiint_{-\infty}^{\infty} R_{u_i u_j}(\rho_x, \rho_z, \tau) e^{-i(\rho_x k_x + \rho_z k_z + \tau \omega)} d\rho_x d\rho_z d\tau$$
$$(2)$$

$$R_{u_i u_j}(\rho_x, \rho_z, \tau)$$
$$= \iiint_{-\infty}^{\infty} \Theta_{u_i u_j}(k_x, k_z, \omega) e^{i(\rho_x k_x + \rho_z k_z + \tau \omega)} dk_x dk_z d\omega \quad (3)$$

k_x and k_z are the streamwise and spanwise wavenumbers, respectively, and ω is the angular frequency. The Fourier transform pair is defined as above to allow for proper normalization of the spectrum, where the normalization is defined by combining Eqs. 1 and 3 at zero shift in time and space as given in Eq. 4.

$$R_{u_i u_j}(0, 0, 0) = \langle u_i u_j \rangle = \iiint_{-\infty}^{\infty} \Theta_{u_i u_j}(k_x, k_z, \omega) dk_x dk_z d\omega \quad (4)$$

In practice, the auto-spectrum is calculated as the square magnitude of the finite Fourier transform of the velocity fluctuations and is normalized using Eq. 4.

2D spectra can be calculated by integration of the 3D spectrum over one dimension as shown in Eq. 5 (where the limits are finite in practice) or by calculating the finite Fourier Transform of a 2D subset of the original 3D sample records and taking an ensemble average over all subsets.

$$\Phi_{u_i u_j}(k_1, k_2) = \int_{-\infty}^{\infty} \Theta_{u_i u_j}(k_1, k_2, k_3) dk_3 \quad (5)$$

k_1, k_2, and k_3 are any three wave vectors. Similarly, 1D spectra can be calculated as the integral of a 2D spectrum or by using a 1D subset of the original 3D dataset and ensemble averaging over all subsets.

As discussed by Adrian (1988), the velocity measured by the PIV algorithm, $\tilde{U}_i(x, y, z, t)$, is not the velocity at a single point in the flow, $U_i(x, y, z, t)$, but the velocity signal averaged over the laser sheet thickness (~ 1 mm) and convolved with a rectangular window, $h(x, z)$, which represents the averaging effect of an interrogation window. The relation between the measured and the true velocity is given in Eq. 6, and the measured fluctuating velocity is defined in Eq. 7.

$$\tilde{U}_i(x, y, z, t) = \left[\int_{y-y_0/2}^{y+y_0/2} U_i(x, y', z, t) dy' \right] \times h(x, z) \quad (6)$$

$$\tilde{u}_i(x, y, z, t) = \tilde{U}_i(x, y, z, t) - \overline{U}_i(y) \tag{7}$$

U is the instantaneous velocity, u is the fluctuating velocity, the star represents convolution, and the overbar indicates an average over all space, time, and experiments that closely approximates the true mean as discussed by Tomkins and Adrian (2005).

The spatial averaging from the interrogation window, h, greatly attenuates fluctuations smaller than two window widths and will also attenuate scales near this limit to a lesser extent. This, then, leads to an attenuation of the measured mean square fluctuations and the velocity spectrum.

When considering the measured velocity signal, $\tilde{u}$, given in Eq. 7, a different spectrum will result. The square magnitude of the Fourier transform of Eq. 7 is given in Eq. 8, where the convolution theorem has been used to separate out the effects of smoothing from the interrogation window.

$$\tilde{\Theta}_{u_i u_j}(k_x, k_z, \omega) = \Theta_{u_i u_j}(k_x, k_z, \omega)\Gamma(k_x, k_z)$$
$$\Gamma(k_x, k_z) = \text{sinc}^2\left(\frac{W_x}{2}k_x\right)\text{sinc}^2\left(\frac{W_z}{2}k_z\right) \tag{8}$$

$\tilde{\Theta}$ is the 3D power spectrum of the measured velocity signal, Γ is the square magnitude of the Fourier transform of the rectangular window, h, and W is the PIV interrogation window size in either x or z as denoted by the subscript. The measured spectrum, $\tilde{\Theta}$, should be normalized by the measured mean square value of the velocity fluctuations, which is the mean square value of the fluctuations defined in Eq. 7.

The effect of Γ is to attenuate the spectrum, particularly at high wavenumbers, where the amplitude of Γ goes to zero at $k = 2\pi/W$. Since Γ is known, one could recover the original spectrum, Θ simply by dividing by Γ, although, in practice, this does not work where Γ approaches zero. As noted by Foucaut et al. (2004), the attenuation becomes significant (more than 50% attenuation) above a wavenumber $k_{\text{cut}} = 2.8/W$. Following their criterion, all data beyond this cutoff will be ignored.

Since the experimental data are not periodic and of finite length, the data are windowed prior to calculating the Fourier transform to prevent spectral leakage. A 3D Hanning window, an extension of the 2D Hanning window used by Tomkins and Adrian (2005), is used here. With the current data, the effect of leakage is most prevalent at the low-frequency end of the spectrum. Multiplying the measured signal by the 3D Hanning window, denoted by g, provides an estimate of the spectrum as presented in Eq. 9.

$$\hat{\tilde{\Theta}}_{u_i u_j}(k_x, k_z, \omega) = \left[[(U_i H) \times G]\,[(U_j^* H^*) \times G^*]\right] \tag{9}$$

The hat indicates that this is an estimate of the spectrum since the signal is windowed and of finite length, the capital letters are the finite Fourier transform of the corresponding lower case quantity where $UU^* = \Theta$, $HH^* = \Gamma$, and the asterisk represents the complex conjugate. Estimates of the 2D and 1D spectra can be calculated as before, and the mean square fluctuations are the same as for the non-windowed data using a proper weighting of the windowing function.

The division of this estimate of the spectrum by Γ to correct the high wavenumber range gives a reasonable estimate of the true spectrum since the convolution with G in spectral space mainly affects the low-frequency/wavenumber range. The same operations were performed by Tomkins and Adrian (2005). In presenting the spectra, both the corrected form (divided by Γ) and the uncorrected form will be shown to illuminate the effects of this correction.

To avoid spatial aliasing, interrogation windows with 50% overlap were used which attenuate aliased energy content above the Nyquist frequency. To avoid temporal aliasing, the data were oversampled during recording, low-pass filtered, and then subsampled before calculating the spectrum as discussed by Wernet (2007). The low-pass filter cutoff for the time signal is set so that $\omega_{\text{cut}} = \overline{U}(y)k_{\text{cut}}$.

To summarize, small-scale features of the flow are attenuated by the averaging over the PIV interrogation window, and large-scale features are smoothed out by spectral leakage. To account for these issues and prevent aliasing, the data are recorded at a higher sampling rate than necessary and the vector fields are calculated using 50% overlap of the interrogation windows. Before any calculations are performed, the data are low-pass filtered in time to get rid of unwanted noise. Prior to calculation of the spectrum, the signal is split into subsets (split twice in z and thrice in time with each region overlapping by 50%) and windowed using a Hanning window to help reduce spectral leakage. Finally, the finite Fourier transform of each subset is calculated, all calculations are averaged, and the data are divided by the smoothing function Γ to get an estimate of the true spectrum Θ where data beyond the cutoff in k_x and k_z are ignored. 1D and 2D spectra are calculated by integration of the resulting 3D spectrum.

5 Spectral energy distributions

We begin this section with a discussion of the symmetries present in the 1D, 2D, and 3D streamwise velocity spectra and the proper normalization of each before moving on to present the 1D, 2D, and 3D spectra calculated from the PIV measurements. Due to a lower than desirable dynamic range of the spanwise velocity fluctuations, neither the spanwise velocity spectrum nor the streamwise–spanwise velocity cross-spectrum will be presented here. For this reason, in the remainder of this document, the $u_i u_j$ subscript for the spectra will be dropped since all spectra will be streamwise velocity spectra.

The 3D auto-spectrum is even and real, which provides symmetry about any coordinate plane if the spectrum is rotated by 180° about the origin, and thus only 4 independent octants exist. Similarly, all 2D spectra are even and real with rotational symmetry about the origin and thus, have only 2 independent quadrants each. Therefore, any 2D spectra can be represented by any half plane and the 3D spectrum by any 4 connected octants. In this half space representation, the magnitude of the spectra is doubled to conserve energy. The 2 non-redundant quadrants of each 2D spectrum are shown in Fig. 4a–c, and the four non-redundant octants (choosing $\omega > 0$) of the 3D spectrum are shown in Fig. 5 for one wall normal location.

From Fig. 4b, c, only a very slight asymmetry is noted in k_z which arises from poorer resolution in this direction as well as slight tilting of the PIV cameras, although some corrections have been made for the latter. For all practical
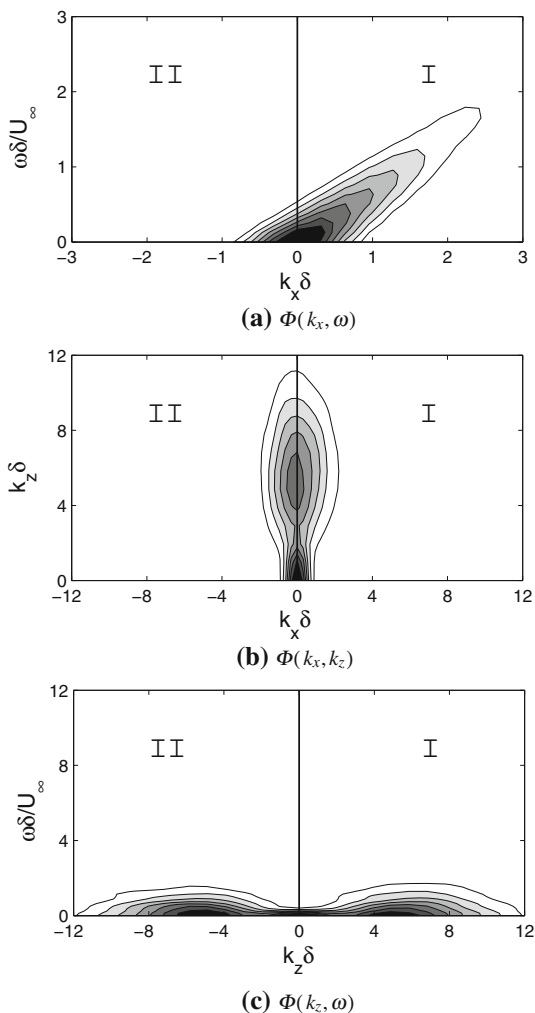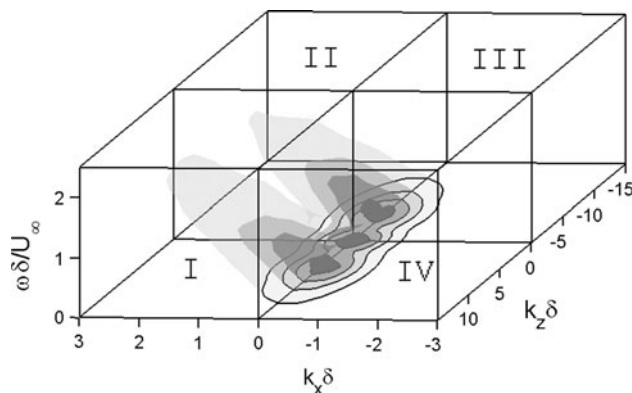

Fig. 5 The half space representation of $\Theta(k_x, k_z, \omega)$ at $y^+ = 108$ is shown, where the spectra in other planes are qualitatively similar. The levels are from 15 to 75% of the maximum energy in 20% increments moving from *light* to *dark shades*. The intersection of the spectrum with $\omega = 0$ is denoted by *solid black lines* to better illuminate the shape of the spectrum

purposes, these spectra are symmetric in k_z. For $\Phi(k_z, \omega)$ this symmetry arises since there is no mean spanwise flow and thus no spanwise directional preference. For $\Phi(k_x, k_z)$ there should physically be no distinction between the positive and negative wavenumber pairs. Thus, both of these spectra can be represented in one quadrant with the magnitude doubled to conserve energy.

For $\Phi(k_x, \omega)$ the two quadrants are not equivalent, where quadrant I is interpreted as downstream traveling waves and quadrant II as upstream traveling waves. The amount of energy in quadrant II is not negligible (at $y^+ = 108$ quadrant II represents about 12% of the total area under the spectrum) as originally suggested by Morrison and Kronauer (1969), and it is necessary to use both planes when integrating $\Phi(k_x, \omega)$ to recover $\Phi(k_x), \phi(\omega)$, or any other integral quantities; otherwise, a low wavenumer spectral distortion will result.

For the 3D spectrum shown in Fig. 5, the same symmetry exists in k_z and the same asymmetry exists in k_x as might be expected from the 2D spectral plots. Thus, the spectrum can be represented by the two octants covering all k_x and positive k_z and ω with the magnitude doubled to preserve the normalization as given in Eq. 5.

$$
\begin{aligned}
\overline{u^2} &= \iiint\limits_{-\infty}^{\infty} \Theta(k_x, k_z, \omega)\mathrm{d}k_x\mathrm{d}k_z\mathrm{d}\omega \\
&= 4 \iiint\limits_{0}^{\infty} [\Theta(k_x, k_z, \omega) + \Theta(-k_x, k_z, \omega)]\mathrm{d}k_x\mathrm{d}k_z\mathrm{d}\omega \\
&= 4 \iiint\limits_{-\infty}^{\infty} k_x k_z \omega [\Theta(k_x, k_z, \omega) + \Theta(-k_x, k_z, \omega)] \\
&\quad \times \mathrm{d}\ln k_x\, \mathrm{d}\ln k_z\, \mathrm{d}\ln \omega
\end{aligned}
\tag{10}
$$

(a) $\Phi(k_x, \omega)$

(b) $\Phi(k_x, k_z)$

(c) $\Phi(k_z, \omega)$

Fig. 4 The *panels* show the half space representation of each 2D spectrum at $y^+ = 108$. The spectra at other wall normal locations are qualitatively similar. The levels shown are from 20 to 80% of the maximum energy in 10% increments moving from *light* to *dark shades*

While the energy in the upstream traveling waves is non-negligible and must be included for proper normalization of $\Theta(k_x, k_z, \omega)$, it is customary in the literature to only plot data for positive streamwise wavenumber, k_x, when these spectra are presented in premultiplied form. While this may seem wrong at first, when premultiplied and presented in log coordinates, the energy in the first decade, which encompasses the upstream traveling waves, is spread out while the remaining 80% of the energy in the second decade is concentrated and, when

considering absolute energy levels, appears much more energetic. Therefore, for the energy levels shown in the following figures, the upstream traveling waves do not appear so plots are presented over positive k_x only.

5.1 1D spectra

Figure 6a, c and e show the 1D premultiplied streamwise velocity spectrum over streamwise wavenumber, spanwise wavenumber, and frequency, respectively, for the

Fig. 6 1D premultiplied streamwise velocity spectra over **a, b** streamwise wavenumber, **c, d** spanwise wavenumbers, and **e, f** frequency. The *solid line* is for $y^+ = 34$, the (+) is for $y^+ = 108$, and the *circle* is for $y^+ = 278$. The uncorrected data are shown in the *left column* and the corrected data are in the *right column*. For the uncorrected data, the *dashed lines* indicate data beyond the imposed cutoff, k_{cut}, beyond which the data begins to be attenuated

(a) $k_x \phi(k_x)$

(b) $k_x \phi(k_x)$

(c) $k_z \phi(k_z)$

(d) $k_z \phi(k_z)$

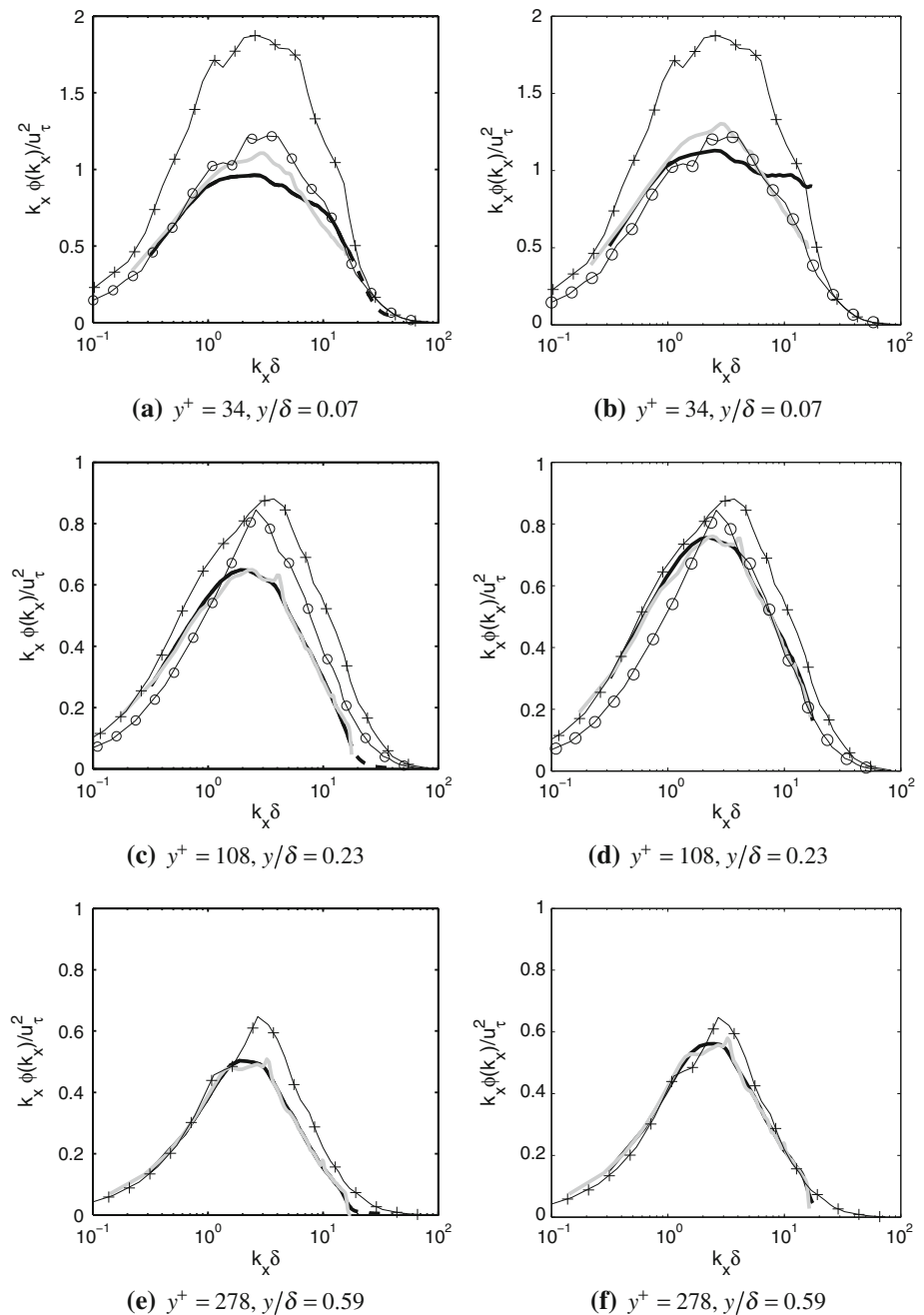**(e)** $\omega \phi(\omega)$

(f) $\omega \phi(\omega)$
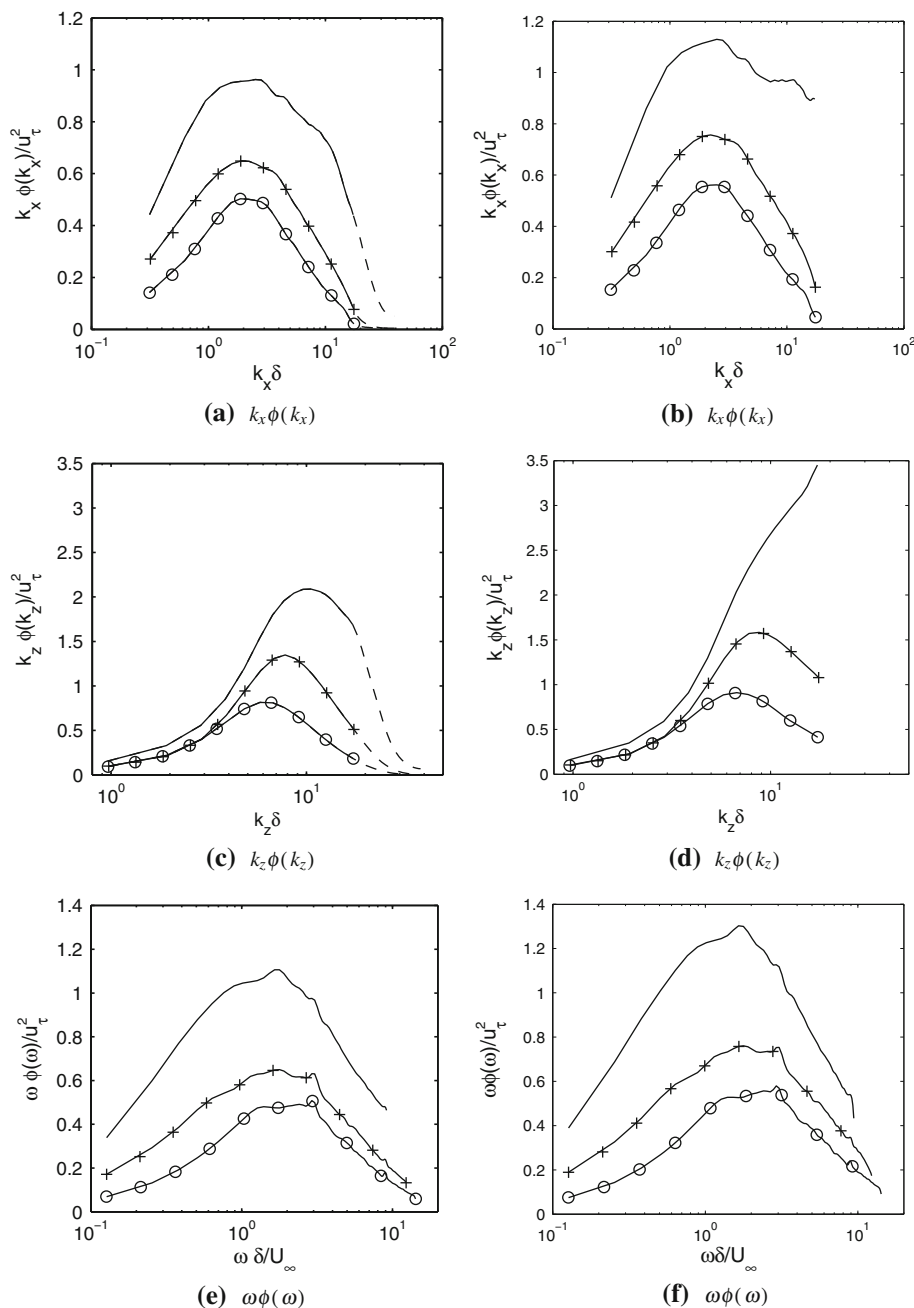
uncorrected data. The corrected data are shown in Fig. 6b, d and f for comparison. The peak in the spectrum over spanwise wavenumber moves to lower k_z (larger spanwise scales) when moving away from the wall indicating that the signature of the dominant scales is growing in spanwise extent in this direction. This has also been shown in the channel flow computations of Jiménez et al. (2004) and boundary layer experiments of Tomkins and Adrian (2005), among others. In the present data, as the peak moves to higher k_z closer to the wall, a larger energetic

portion of the spectrum is cut off by spatial averaging. In fact, at $y^+ = 34$, a better resolution would be required to resolve the peak in the spectrum over spanwise wavenumbers. Therefore, any integral quantities in the z direction, including the rms velocity fluctuations and spectra, will be more in error as the wall is approached. This is likely the reason for the slight underestimation of u_{rms} at $y^+ = 34$ shown in Fig. 3b.

In Fig. 7, the 1D spectra over frequency and over streamwise wavenumber are compared to one another

Fig. 7 The streamwise wavenumber and frequency spectra are compared where the colors are *black*: $k_x\phi(k_x)$, *gray*: Taylor conversion of $\omega\phi(\omega)$. The uncorrected data are shown in the *left column* and the corrected data are in the *right column*. For the uncorrected data, the *dashed lines* indicate data beyond the imposed cutoff, k_{cut} beyond which the data begins to be attenuated. Data from Erm and Joubert (1991) at $Re_\theta = 1{,}020$ is represented by *symbols* where the wall normal locations are **a, b** $y/\delta = 0.04$ (+), 0.1 (*circle*), **c, d** $y/\delta = 0.2$ (+), 0.35 (*circle*), and **e, f** $y/\delta = 0.55$ (+)

(a) $y^+ = 34$, $y/\delta = 0.07$

(b) $y^+ = 34$, $y/\delta = 0.07$

(c) $y^+ = 108$, $y/\delta = 0.23$

(d) $y^+ = 108$, $y/\delta = 0.23$

(e) $y^+ = 278$, $y/\delta = 0.59$

(f) $y^+ = 278$, $y/\delta = 0.59$

using Taylor's hypothesis and to the hotwire measurements of Erm and Joubert (1991) at a similar Reynolds number and comparable wall normal locations. The 1D spectra are in fair agreement with the data of Erm and Joubert (1991), and this agreement is improved when the data are corrected as shown in the plots in the right column of Fig. 7. This improved agreement with the corrected 1D spectra should also be indicative of a proper correction for the 2D and 3D spectra as the correction is applied to the 3D spectrum, and all other spectra are calculated via integration of this spectrum. The only major deviation between the temporal and spatial spectra is at $y^+ = 34$. This deviation may be indicative of the variation of the convection velocity of scales from the local mean, although noise may also be contributing to this variation, particularly at the high k_x end, as shown in the 2D spectra in Sect. 2. Some error may be expected at this wall normal location since there is a slight deviation of the mean velocity profile from the measurements of DeGraaff and Eaton (2000) as shown in Fig. 3a, and thus, other statistics may be adversely affected. For the other two planes, there is almost no deviation between the spatial and Taylor converted temporal spectra, indicating that the frozen flow assumption should hold at these locations.

5.2 2D spectra

The 2D premultiplied $\Phi(k_x, \omega)$ streamwise velocity spectra, i.e. $k_x \omega \Phi(k_x, \omega)$, are shown for each plane in Fig. 8 with the uncorrected data in the left column and the corrected data in the right column. Note that in the 1D spectra of Fig. 6, the maximum energy of each spectrum decreases as measurements are taken further from the wall, as expected. In the 2D plots here and 3D plots to follow, contour levels represent a fraction of the maximum energy of each individual spectrum so this variation will not be present. Also, note that the total energy of a spectrum is different before and after correction, so the levels shown for the uncorrected spectra do not represent the same levels shown for the corrected spectra.

One notable difference between the corrected and uncorrected $k_x \omega \Phi(k_x, \omega)$ is the apparent noise that appears in the corrected spectrum in the range of $7 < k_x \delta < 20$ and $1 < \omega \delta / U_\infty < 9$. In this same high wavenumber range, there is a discrepancy between the spatial and temporal 1D spectrum as shown in Fig. 7a and more prevalently in the corrected spectrum in Fig. 7b where the amplitude of the spatial spectrum exceeds the temporal spectrum. Since the 1D temporal and streamwise wavenumber spectra should agree for the nearly homogeneous small scales, the discrepancy beyond $k_x \delta = 7$ likely comes from noise. It is hypothesized that this noise in the near wall plane is from the measurement of nearly stationary particles or bubbles

that clustered near the surface and were illuminated by the laser sheet during PIV acquisition.

From $\Phi(k_x, \omega)$, a convection velocity can be calculated for each streamwise scale as shown in Fig. 9. The method of finding the ridge line, the line of maxima along the spectrum as outlined by Goldschmidt et al. (1981), is used here where the convection velocity is then defined as ω / k_x along the ridge line (the solid line in the Fig. 9). For the plane shown at $y^+ = 34$, it is apparent that most scales travel faster than the local mean velocity. This is in fair agreement with Krogstad et al. (1998), whose data from hotwire measurements are presented for comparison. The discrepancy beyond $k_x \delta = 7$ may again be affected by the noise in this region as described previously, and for this reason, data beyond this point in Fig. 9 have been denoted by a dashed line. In addition, the slow convection velocities for low wavenumbers reflect the lack of scale separation at this low Reynolds number, namely the dominance of the near-wall structures over the superstructures which are centered at locations further from the wall but inhabit a similar wavenumber range.

Premultiplied $\Phi(k_z, \omega)$ and $\Phi(k_x, k_z)$ are shown for each plane in Figs. 10 and 11, respectively. The uncorrected data are shown in the left column and the corrected data are shown in the right column. In addition, data from the channel flow computations presented by del Álamo and Jiménez (2001) at $y^+ = 90$ and $Re_\tau = 550$ are included for comparison to the current data at $y^+ = 108$ to validate the correction applied (some differences are expected due to the difference in geometry between these two flows as well as the slight difference in Reynolds number and wall normal location). The correction appears to push the spectral peak in the right direction and aligns the current data to the data from del Álamo and Jiménez (2001). The dotted contours for the uncorrected data show the region that is beyond the wavenumber cutoff and again show that the resolution in z is not sufficient to resolve the peak in the spanwise direction at $y^+ = 34$. Again, the correction pushes the peak in the spectra to higher k_z and increases the energy in the spectra in general near this cutoff. Upon integration in k_z, the resulting corrected 1D spectra will have a higher level throughout than the uncorrected spectra, as evidenced in the $\phi(k_x)$ and $\phi(\omega)$ plots in Fig. 7.

$\Phi(k_x, k_z)$ shows some variability between the three planes, becoming less elongated in streamwise wavenumber further from the wall as shown in Fig. 11a, c and e. The range of energetic streamwise scales narrows while the range of spanwise scales remains fairly constant moving further from the wall leading to a more homogeneous distribution of the energy in the wake region.

Note that all 2D spectra show that the range of streamwise scales becomes smaller and the larger streamwise scales become less dominant beyond the log layer.

Fig. 8 $k_x \omega \Phi(k_x, \omega)$ is presented for all three planes. The uncorrected data are presented in the *left column* and the corrected data are in the *right column*. For each plot, the contours represent 20–80% of the maximum energy of the spectrum moving from *lighter* to *darker shades* in 10% increments

(a) $y^+ = 34$

(b) $y^+ = 34$

(c) $y^+ = 108$

(d) $y^+ = 108$

(e) $y^+ = 278$

(f) $y^+ = 278$
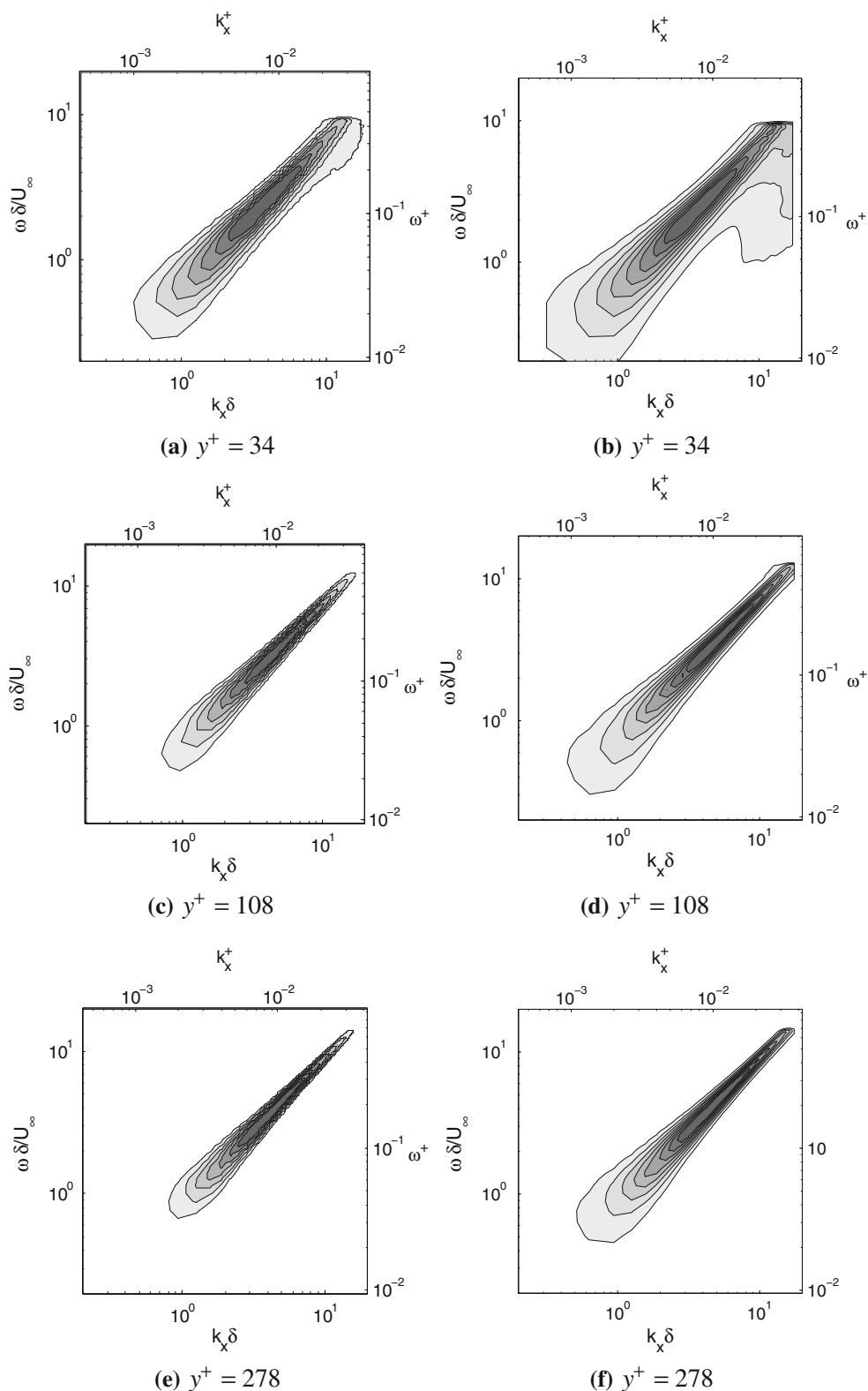
Recall, that these conclusions are drawn upon low Re data so the scale separation is not large, yet this conclusion about the change in scale size from the inner layer to the

wake region should apply to higher Reynolds number data. This illustrates the difficulty in performing PIV in planes near the wall as the range of energetic scales is broader,
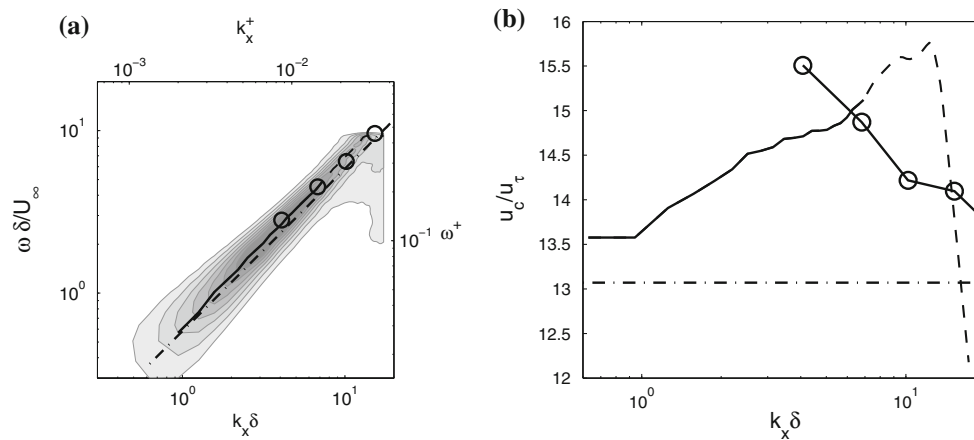
Fig. 9 **a** The convection velocity calculated by finding the line of local maxima along $k_x \omega \Phi(k_x, \omega)$ at $y^+ = 34$ is indicated by the *solid black line* (*dashed black line* beyond the point where noise influences the calculation) and displayed on *top* of the spectrum where the contours represent 20–80% of the maximum energy of the spectrum moving from *light* to *dark shades* in 10% increments. The *dash-dot line* indicates where $\omega = \overline{U} k_x$ signifying a convection velocity equal to the local mean. The *four open circles* are data from Krogstad et al.

(1998) at the same y^+ and similar Reynolds number. These data were converted from their original form, convection velocity plotted against streamwise probe separation, by converting the separation to a wavenumber and using the convection velocity for each wavenumber to define an associated frequency. (**b**) The convection velocity is plotted as a function of wavenumber where the *lines and symbols* are the same as in **a**

and large scales play a more dominant role. Thus, both a very large field of view and a very fine resolution are needed, which was difficult to achieve in the current experiment. The best solution is to analyze both a large field to obtain the large-scale features and a small, well-resolved field from which a composite spectrum can be produced covering the whole wavenumber range, which is the focus of future experiments.

5.3 3D spectra

Finally, two views of the 3D premultiplied streamwise velocity spectra, $k_x k_z \omega \Theta(k_x, k_z, \omega)$, are presented in each wall parallel plane in Fig. 12a–f for the corrected data. The uncorrected data have been omitted since differences between the two are already clearly outlined by the 2D spectra in Sect. 2. The cutoff of each spectrum is clearly shown here, and the effect of this cutoff on all of the spectra presented so far can easily be understood by considering an integration in one or more coordinate directions.

These three-dimensional spectra show not only the energy distribution over all scales, but over all scales traveling at all velocities, where the convection velocity of a scale is defined as $u_{c,x} = \omega/k_x$. In this framework, if the flow is decomposed into traveling waves as in the model of McKeon and Sharma (2010), then the spectra are the footprints of these waves at particular wall normal locations. For flow control applications, measurements taken at several wall normal locations would provide a well-characterized response of the boundary layer to a periodic

excitation (as studied in Jacobi et al. (2010) and Jacobi and McKeon (2011) using hotwires), and alterations of the spectra could be used to see how a particular input restructures the flow. Such information could be used for optimal control design.

To gain insight into the convection velocity of different scales in the flow, a single convection velocity can be calculated for each streamwise and spanwise scale pair from the three-dimensional spectra using Eq. 11 from del Álamo and Jiménez (2009) and used in earlier works by Jiménez et al. (2004) and Flores and Jiménez (2006).

$$u_c(k_x, k_z, y) = \frac{1}{k_x} \frac{\int_{-\infty}^{\infty} \omega \Theta(k_x, k_z, \omega, y) \mathrm{d}\omega}{\int_{-\infty}^{\infty} \Theta(k_x, k_z, \omega, y) \mathrm{d}\omega} \tag{11}$$

This convection velocity definition uses a value of ω that is weighted by the 3D streamwise velocity spectrum. In this way, it gives the dominant convection velocity for each streamwise–spanwise scale pair. A map of the convection velocity is presented in Fig. 13 where lines of constant convection velocity are plotted on top of $k_x k_z \Phi(k_x, k_z)$ to highlight the convection velocity of the most energetic scales. From this chart, it is apparent that most scales at $y^+ = 34$ travel slower than the local mean except for the large scales in the range $2 < \lambda_x/\delta < 5$. This differs from the trend in Fig. 9 where almost all scales recovered traveled faster than the local mean. This difference may be expected as the method of calculating the convection velocity differs between the two figures where one searches for a maximum (method for Fig. 9) while the other looks for a "center of

Fig. 10 $k_z \omega \Phi(k_z, \omega)$ is presented for all three planes where the contours represent 20–80% of the maximum energy of the spectrum moving from *light* to *dark shades* in 10% increments. The uncorrected data are presented in the *left column* and the corrected data are in the *right column*. For the uncorrected data, the *unshaded* contours are regions of the spectrum beyond the streamwise and spanwise cutoff, k_{cut}, that may be irregularly shaped due to spectral attenuation, but are included for visualization

(a) $y^+ = 34$

(b) $y^+ = 34$

(c) $y^+ = 108$

(d) $y^+ = 108$

(e) $y^+ = 278$

(f) $y^+ = 278$
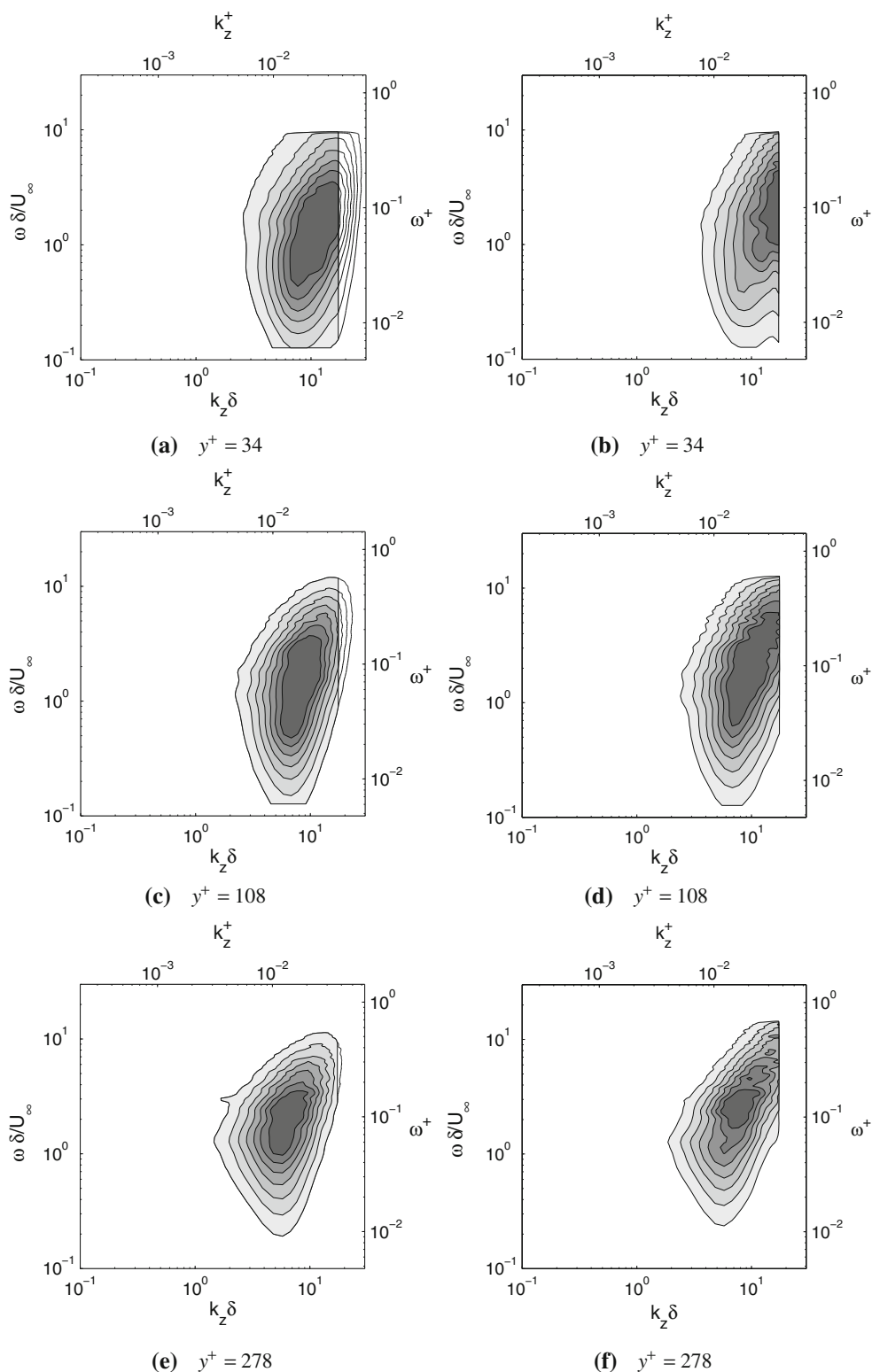
mass" (method for Fig. 13). Also, the noise that exists over a range of ω as well as the cutoff imposed in ω will manifest itself differently when using an integral method such as Eq.

11. An investigation of such convection velocity maps, as well as the definition of convection velocities in general, is a subject of future work.

Fig. 11 $k_x k_z \Phi(k_x, k_z)$ is presented for all three planes where the contours represent 20–80% of the maximum energy of the spectrum moving from *light* to *dark shades* in 10% increments. The uncorrected data are presented in the *left column* and the corrected data are in the *right column*. For the uncorrected data, the *unshaded* contours are regions of the spectrum beyond the streamwise and spanwise cutoff, k_{cut}, that may be irregularly shaped due to spectral attenuation, but are included for visualization. Linearly spaced spectral contours from del Álamo and Jiménez (2001) for a channel flow computation at $Re_\tau = 550$ at $y^+ = 90$ are shown with *circles* where *cool colors* indicate less energetic portions of the spectrum. This is compared to the current data in **c** and **d** to show the validity of the correction

(a) $y^+ = 34$

(b) $y^+ = 34$

(c) $y^+ = 108$

(d) $y^+ = 108$

**(e)** $y^+ = 278$

(f) $y^+ = 278$
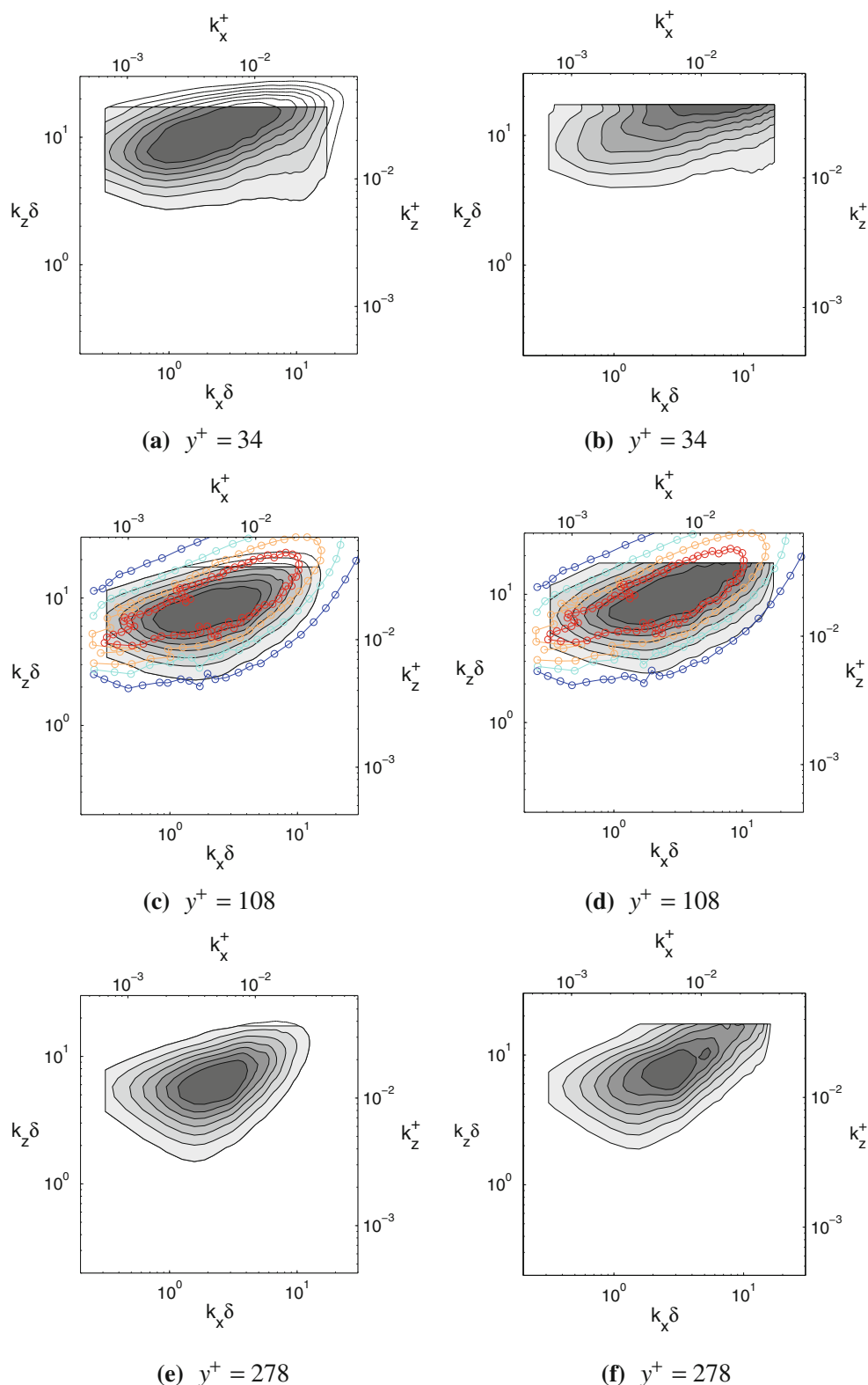
6 Conclusions

We presented for the first time 3D streamwise velocity power spectra (2D in space and 1D in time) in all regions of

the turbulent boundary layer and outlined the method for calculating and normalizing these from PIV measurements. The effect of the PIV interrogation window on the resolution and attenuation of both the spectrum and the

Fig. 12 $k_x k_z \omega \Theta(k_x, k_z, \omega)$ is presented at each wall normal location. The surfaces represent 25, 50, and 75% of the total energy in each spectrum moving from *light* to *dark shades*. The *left* and *right columns* offer two different views. Data beyond the k_x and k_z cutoffs are not shown

(a) $y^+ = 34$

(b) $y^+ = 34$

(c) $y^+ = 108$

(d) $y^+ = 108$

(e) $y^+ = 278$

(f) $y^+ = 278$
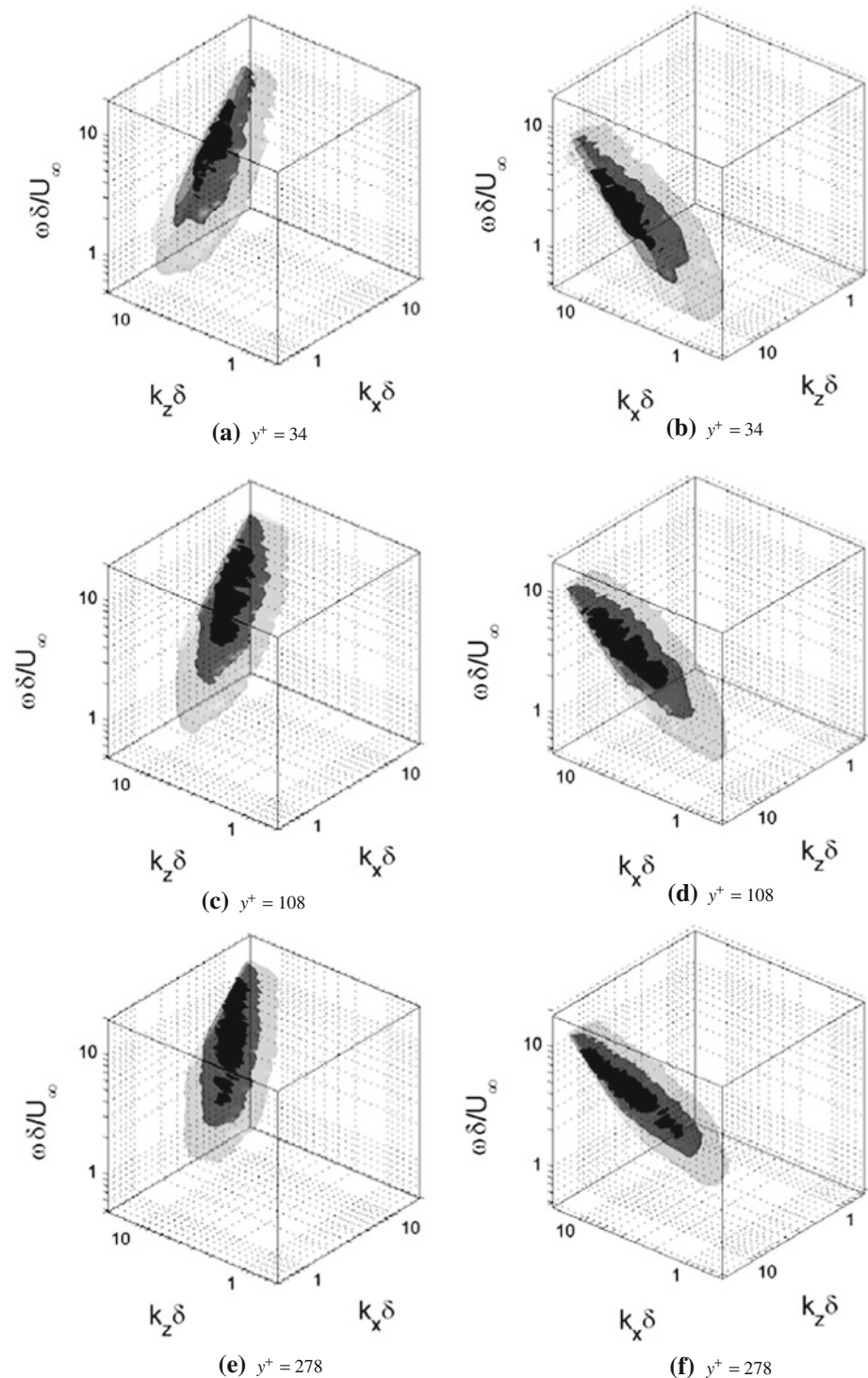
measured velocity fluctuations was discussed. In addition, the methods used for reducing aliasing and spectral leakage were outlined. From the 3D spectra presented, the more usual 1D and 2D spectra were also calculated and compared with previous findings.

With the current dataset, it was found that the spanwise resolution of the streamwise velocity fluctuations was lacking, while the streamwise and temporal resolutions were reasonable. Current experiments are underway to improve the spanwise resolution and also to increase the dynamic range to improve the resolution of spanwise fluctuations so that the spanwise and streamwise–spanwise cross-spectrum can be analyzed. Regardless of these issues, it was still possible to consider the convection velocity of
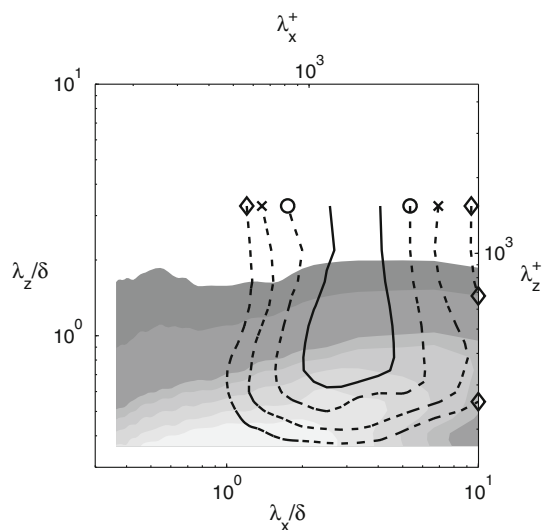
Fig. 13 The *contour lines* represent the convection velocity at $y^+ = 34$ using the method outlined in Eq. 11 where *solid contours* denote a convection velocity equal to the local mean and *dotted contours* with symbols are convection velocities below the local mean where the symbols are: *circle* $\overline{U}^+ - u_\tau$; x: $\overline{U}^+ - 2u_\tau$; *diamond* $\overline{U}^+ - 3u_\tau$. The *shaded contours* represent 20–80% of the maximum energy of $k_x k_z \Phi(k_x, k_z)$ in 10% increments moving from *light* to the *dark shades*

streamwise scales over both streamwise and spanwise wavenumbers using the calculated 3D spectrum. The investigation and interpretation of these is an area of current interest.

References

Adrian RJ (1988) Statistical properties of particle image velocimetry measurement in turbulent flow. In: Laser anemometry in fluid mechanics III, pp 115–129

Balakumar BJ, Adrian RJ (2007) Large- and very-large-scale motions in channel and boundary-layer flows. Philos Trans R Soc A 365:665–681

Bobba KM (2004) Robust flow stability: theory, computations and experiments in near wall turbulence. PhD thesis, California Institute of Technology

Chung D, McKeon BJ (2010) Large-eddy simulation of large-scale structures in long channel flow. J Fluid Mech 661:341–364

DeGraaff DB, Eaton JK (2000) Reynolds-number scaling of the flat-plate turbulent boundary layer. J Fluid Mech 422:319–346

del Álamo JC, Jiménez J (2001) Direct numerical simulation of the very large anisotropic scales in a turbulent channel. Cent Turbul Res Annu Res Briefs 2001:329–341

del Álamo JC, Jiménez J (2009) Estimation of turbulent convection velocities and corrections to Taylor's approximation. J Fluid Mech 640:5–26

Dennis DJC, Nickels TB (2008) On the limitations of Taylor's hypothesis in constructing long structures in a turbulent boundary layer. J Fluid Mech 614:197–206

Erm LP, Joubert PN (1991) Low-Reynolds-number turbulent boundary layers. J Fluid Mech 230:1–44

Flores O, Jiménez J (2006) Effect of wall-boundary disturbances on turbulent channel flows. J Fluid Mech 566:357–376

Foucaut JM, Carlier J, Stanislas M (2004) PIV optimization for the study of turbulent flow using spectral analysis. Meas Sci Tech 15:1046–1058

Ganapathisubramani B, Longmire EK, Marusic I (2003) Characteristics of vortex packets in turbulent boundary layers. J Fluid Mech 478:35–46

Goldschmidt V, Young M, Ott E (1981) Turbulent convective velocities (broadband and wavenumber dependent) in a plane jet. J Fluid Mech 105:327–345

Guala M, Metzger M, McKeon BJ (2011) Interactions within the turbulent boundary layer at high Reynolds number. J Fluid Mech 666:573–604

Hutchins N, Marusic I (2007) Large-scale influences in near-wall turbulence. Philos Trans R Soc A 365:647–664

Jacobi I, McKeon BJ (2011) Dynamic spatially-impulsive roughness perturbation of a turbulent boundary layer and the excitation of 'critical layer' velocity modes (submitted)

Jacobi I, Guala M, McKeon BJ (2010) Characteristics of a turbulent boundary layer perturbed by spatially-impulsive dynamic roughness. AIAA-2010-4474

Jiménez J, del Álamo JC, Flores O (2004) The large-scale dynamics of near-wall turbulence. J Fluid Mech 505:179–199

Keane RD, Adrian RJ (1990) Optimisation of particle image velocimeters-part I: double pulsed systems. Meas Sci Technol 1:1202–1215

Kim J, Hussain F (1993) Propagation velocity of perturbations in turbulent channel flow. Phys Fluids A 5(3):695–706

Kim KC, Adrian RJ (1999) Very large-scale motion in the outer layer. Phys Fluids 11(2):417–422

Krogstad PA, Kaspersen JH, Rimestad S (1998) Convection velocities in a turbulent boundary layer. Phys Fluids 10(4):949–957

LeHew J, Guala M, McKeon BJ (2010) A study of convection velocities in a zero pressure gradient turbulent boundary layer. AIAA-2010-4474

McKeon BJ, Sharma AS (2010) A critical layer model for turbulent pipe flow. J Fluid Mech 658:336–382

Monty JP, Chong MS (2009) Turbulent channel flow: comparison of streamwise velocity data from experiments and direct numerical simulation. J Fluid Mech 633:461–474

Monty JP, Hutchins N, Ng HCH, Marusic I, Chong MS (2009) A comparison of turbulent pipe, channel and boundary layer flows. J Fluid Mech 632:431–442

Morrison WRB, Kronauer RE (1969) Structural similarity for fully developed turbulence in smooth tubes. J Fluid Mech 39:117–141

Morrison WRB, Bullock KJ, Kronauer RE (1971) Experimental evidence of waves in the sublayer. J Fluid Mech 47:639–656

Spalding DB (1961) A single formula for the law of the wall. Trans ASME E 28:455–458

Taylor GI (1938) The spectrum of turbulence. Proc R Soc Lond A 164:476–490

Tomkins CD, Adrian RJ (2005) Energetic spanwise modes in the logarithmic layer of a turbulent boundary layer. J Fluid Mech 545:141–162

Wernet MP (2007) Temporally resolved PIV for space-time correlations in both cold and hot jet flows. Meas Sci Technol 18:1387–1403

Willert CE, Gharib M (1991) Digital particle image velocimetry. Exp Fluids 10:181–193